

Wettability-Driven Assembly of Electrochemical Microsupercapacitors

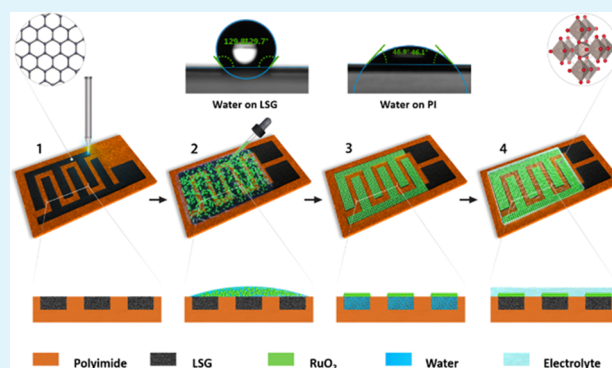
Wenli Zhang,^{ID} Qiu Jiang, Yongjiu Lei, and Husam N. Alshareef^{*ID}

Materials Science and Engineering, Physical Science and Engineering Division, King Abdullah University of Science and Technology (KAUST), Thuwal 23955-6900, Saudi Arabia

Supporting Information

ABSTRACT: In this work, we demonstrate a wettability-driven assembly (WDA) process of active particulate materials for microsupercapacitor (MSC) fabrication. Our process uses three-dimensional laser-scribed graphene (LSG), derived from polyimide, as a current collector. We exploit the drastic wettability difference between LSG and unconverted polyimide toward water to assemble various electrodes on the LSG collectors. The WDA process is demonstrated using porous carbon and RuO₂ nanoparticles, which are spontaneously and selectively assembled onto the LSG finger electrodes. The MSCs assembled using the WDA process with porous carbon as active material deliver a much higher areal capacitance (41.2 mF cm⁻²) compared to MSCs using LSG-only electrodes (1.2 mF cm⁻²). Thus, they deliver a high areal energy density of 5.71 μWh cm⁻² with an areal power density of 4.0 mW cm⁻². The capacitance and energy density of these porous carbon MSCs outperform most recently reported carbon-based MSCs. In comparison, the MSCs assembled using the WDA process with RuO₂ nanoparticles as active material deliver an areal capacitance of 70.3 mF cm⁻² and an areal energy density of 9.71 μWh cm⁻². All in all, the WDA process is green, simple, and well suited for the fabrication of MSCs using many types of active materials.

KEYWORDS: laser-scribed graphene, porous carbon, wettability, microsupercapacitor, ruthenium dioxide, graphene



1. INTRODUCTION

Miniaturized energy storage devices have become increasingly important with the fast development of wearable and miniaturized electronics, especially for stand-alone self-powered devices.^{1–3} Thin-film batteries, the so-called microbatteries, have been designed to meet the energy and power requirements of miniaturized electronic applications.⁴ However, the use of these batteries has been restricted due to their short service life and low power density.⁵ In contrast, microsupercapacitors (MSCs) with long cycle life, high reversibility, and moderate cost offer another option for miniaturized energy storage.^{2,6–13} Furthermore, MSCs can be integrated with various types of energy-harvesting devices (photovoltaic cell, piezoelectric or triboelectric generators) because MSCs can absorb a much higher peak current than do microbatteries.¹⁴ In this scenario, MSCs have attracted widespread attention for miniaturized electronics. Despite all of these merits, however, most MSCs show unsatisfactory areal energy densities of less than 1 μWh cm⁻² due to their thin-film design, which hampers their real-world applications.⁷ The areal energy density of an MSC can be improved by proper selection of active materials,¹⁵ current collector/active materials design,^{16–18} and asymmetric configuration design.¹⁹ Developing high-capacitance materials is one effective strategy to improve the areal energy density. Although pseudocapacitive

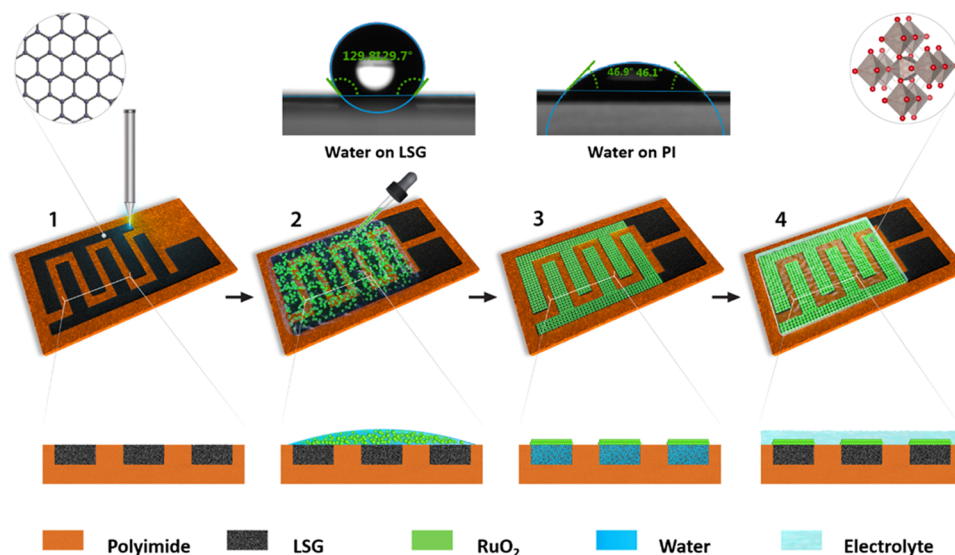
materials with high capacitance^{15,20–22} have been used as active materials in MSCs, porous carbon is still the most reliable active material for supercapacitors.²³ Porous carbon is considered an effective active material for MSCs because it possesses a high surface area (up to 3000 m² g⁻¹), leading to a high gravimetric specific capacitance of up to 300 F g⁻¹.²⁴ In addition, porous carbon is less expensive and exhibits better cycling stability than most pseudocapacitive materials. To fabricate the interdigitated electrode patterns of MSCs, typically the active materials are deposited by inkjet or screen printing,^{25,26} electrophoretic deposition,^{27,28} or electrodeposition,^{21,29,30} followed by photolithography or laser scribing. These well-developed methods are suitable for the fabrication of thin-film electrodes for MSCs. The energy densities of thin-film MSCs are limited by their low mass loading.

To achieve MSCs with high areal energy density, using a three-dimensional (3D) current collector has been demonstrated to be an efficient strategy for thick electrodes. Various 3D substrates have been developed to fabricate MSCs, such as nickel foam, carbon cloth, and porous gold.^{16–18} Using a 3D current collector would achieve not only high mass loading but

Received: March 30, 2019

Accepted: May 17, 2019

Published: May 17, 2019

Scheme 1. Schematic Illustration of the WDA Process Used for Assembly of MSCs^a

^a(1) Laser scribing formation process of LSG patterns, (2) drop-casting of active material slurry onto the top of the LSG/polyimide, (3) WDA process for the fabrication of the MSC, and (4) final assembly of the MSC with H₂SO₄/PVA gel electrolyte. In the illustration, RuO₂ is shown as a typical active material that can be used in the WDA process.

also enable efficient contact between the active material particulates and current collectors. Laser-scribed graphene (LSG) is a class of polycrystalline graphene material derived from the laser irradiation of sp³-carbon-rich carbon sources.^{31,32} LSG can be prepared from various organic precursors, such as amorphous carbon,³³ polyimide,^{21,34–36} graphene oxide,^{37–39} lignin,⁴⁰ paperboard,⁴¹ wood,⁴² and organics.^{43,44} Over the last decade, chemically modified LSGs have been developed for various applications, such as oxygen reduction/evolution reactions,⁴⁵ hydrogen evolution,⁴⁶ sensors,^{46,47} environmental remediation,⁴⁸ electronics,^{49,50} and MSCs.^{35,51} As a 3D porous graphene matrix, LSGs can be used as binder-free electrodes for MSCs. However, due to the low mass loading and the low specific surface area (SSA) of LSG (<500 m² g⁻¹), LSG MSCs exhibit low areal capacitance and energy density (<4 mF cm⁻², ca. 0.4 μWh cm⁻²).³⁵ Although boron-doped LSG has high areal capacitance (16.5 mF cm⁻² for boron-doped LSG), the areal energy density is still low (ca. 2 μWh cm⁻²).⁵² The MoS₂-decorated LSG yields an areal capacitance of only 14 mF cm⁻².⁵³ Most reported MSCs using LSG as electrodes have either low capacitance (<20 mF cm⁻²) or low rate capability. Nevertheless, LSG may be a good current collector to assemble MSCs due to its 3D structure and relatively good conductivity (ca. 5–25 S cm⁻¹).³¹ The 3D structure of LSG could reduce the contact resistance between LSG and active materials. To fabricate pseudocapacitive MSCs, Tour et al. decorated LSG with pseudocapacitive materials (PANi, MnO₂, and FeOOH) using a well-established electrodeposition technology, which obtained high areal energy density (ca. 8 μWh cm⁻²) and good rate performance.²¹

In this paper, we have developed a new wettability-driven assembly (WDA) process for the self-assembly of electrode materials for MSC applications. Our process takes advantage of a drastic difference in the wettability between polyimide and LSG toward water. Using 3D LSG patterns as current collectors, the WDA process spontaneously assembles active materials onto the LSG patterns, which can be universally applied to different electrode materials. Compared to other

traditional fabrication technologies of MSC, WDA is green, simple, and fast, which holds great potential for MSC fabrications. Devices made using this process, details of which are discussed later, show exceptional performance among all previously reported LSG MSCs.

2. RESULTS AND DISCUSSION

We have created an easy WDA process for the assembly of electrochemical MSCs using both electrochemical double-layer capacitors active material, porous carbon, and pseudocapacitive active material, RuO₂. The process uses the porous carbons we developed (discussed later) and hydrothermally produced RuO₂ as active materials and LSG as current collector. LSG is a multilayered graphene (Figure S1A, Supporting Information) with a 3D carbon network (Figure S1B).³⁵ Furthermore, LSG is a highly conductive carbonaceous material with a sheet resistance of 11.7 Ω sq⁻¹. Its low resistance enables fast electron transport in LSG, and its 3D porous framework allows high mass loading of active materials. The details of our WDA process are illustrated in Scheme 1. The WDA process comprises the following three easy room-temperature steps: (1) laser scribing of LSG patterns on the polyimide films; (2) dispersing a water-based slurry containing particulates of the active materials onto the surface; and (3) drying the device. First, an LSG interdigitated finger electrode pattern (dimensions are shown in Figure S2) is formed on polyimide films using a direct CO₂ laser scribing technique, which we have previously reported.⁴⁰ After that, a slurry containing water, active materials, sodium carboxymethyl cellulose (CMC), and acetylene black is drop-casted onto the surface of LSG. After a fast vacuum-drying process, the porous carbon particles spontaneously assemble on the LSG collector fingers (Figure S3A,B). A gel electrolyte is then used to coat the finger electrode to finalize the MSC fabrication.

The mechanism of the WDA process can be explained as follows. The LSG and polyimide have different wettabilities toward water: LSG is hydrophobic with a contact angle of 129° due to its low oxygen moieties,³⁵ while polyimide is relatively

hydrophilic with a small contact angle of 46° (Scheme 1) due to its abundance of carbonyl groups. As a result of this wettability difference, drop-casting the water-based slurry on the surface of the LSG/polyimide substrate leads to an interesting behavior. After the casting of the slurry, the water on top of the LSG remains on the surface of the LSG, while the polyimide between the LSG finger electrodes is covered by water. With a fast vacuum-drying process, air in the spaces of 3D LSG goes out; then, the macropores inside the LSG absorb the water from the slurry, while the slurry on polyimide flows onto the top of the 3D LSG finger patterns. Hence, the porous carbon particles spontaneously and uniformly assemble onto the surface of LSG fingers.

To show the wettability contrast as a critical parameter in our proposed WDA process, we tested the method using another solvent: *N*-methyl-2-pyrrolidone (NMP) solvent. Since both LSG and polyimide are lyophilic toward NMP (Figure S4A,B), NMP-based electrode slurry does not work well for MSC assembly (Figure S3C). Instead, after drying, the porous carbon particles covered the entire surface of the LSG/polyimide substrate, including both LSG fingers and polyimide that was not exposed to the laser. Hence, the WDA process is not applicable for organic solvent-based slurries due to its similar wettability behaviors on LSG and PI.

To achieve the high performances of MSC, we have developed porous carbons with either high capacitance or high rate capability from a single carbon source. Generally, porous carbons are produced by well-known chemical activation using renewable biomasses.^{54–57} Chemical activation, using KOH or NaOH as activation agent, can produce porous carbon with high surface area; however, chemical activation generally uses a high amount of activation agent (usually, 3:1 ratio of KOH to char),^{24,58,59} which is costly and polluting. In recent years, direct pyrolysis method has been considered as the second-generation technology for the preparation of porous carbon for supercapacitor applications.^{60,61} Direct pyrolysis approach produces porous carbons with relatively high surface areas and a diversity of morphologies.^{62,63}

To realize our idea, we prepared porous carbon materials from the well-known precursor ethylenediaminetetraacetic acid (EDTA) disodium salt (Figure 1A). By converting two acetate groups into sodium acetates, we can obtain EDTA tetrasodium salt. Then, using this EDTA tetrasodium salt as a precursor, a hierarchical amorphous porous carbon (HAPC) is obtained by direct pyrolysis method. In another approach, EDTA disodium salt is converted into EDTA nickel coordination salt, followed by direct pyrolysis, through which we obtain graphitic carbon nanocages (GCNC).

After the pyrolysis of EDTA tetrasodium salt, the sodium species are transformed into Na_2CO_3 (Figure S5). Na_2CO_3 in the carbon skeleton acts not only as a template but also as an activation agent. The obtained HAPC has 3D macroporous morphology due to the template effect of Na_2CO_3 . The size of macropores inside the HAPC skeleton is around 1–2 μm (Figure 1B), but the wall thickness of HAPC is as thin as 200–300 nm, which ensures effective electrolyte diffusion. The high-resolution transmission electron microscopy (HRTEM) image in Figure 1C shows that HAPC is an amorphous porous carbon with randomly oriented, curly, short-range graphene layers and micropores (Figure 1C). The pyrolysis of EDTA nickel coordination salt results in the formation of spherulike morphology (Figure S6) and nickel metal particles, as shown

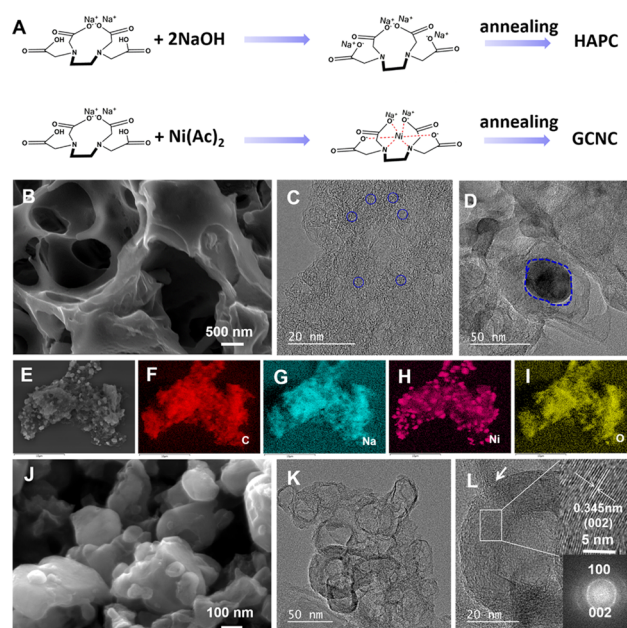


Figure 1. (A) Schematic illustrating the synthesis strategies of HAPC and GCNC; (B) scanning electron microscopy (SEM) image of HAPC; (C) high-resolution transmission electron microscopy (HRTEM) image of HAPC, where the blue circle highlights some micropores inside HAPC; (D) TEM image of the pyrolysis product of EDTA nickel coordination salt (nickel particle is highlighted by a blue dash circle); (E) SEM image and the energy-dispersive X-ray spectroscopy (EDS) element mapping of (F) C, (G) Na, (H) Ni, and (I) O of the pyrolysis product of EDTA nickel coordination salt; (J) SEM image of GCNC; (K) TEM image of GCNC; and (L) HRTEM of GCNC, where insets are HRTEM and the corresponding fast Fourier transform image.

in Figure 1D (verified by X-ray diffraction (XRD) pattern in Figure S5 and HRTEM image in Figure S7). The sodium species in EDTA nickel coordination salt are transformed into Na_2CO_3 during pyrolysis, which is confirmed by energy-dispersive X-ray spectroscopy (EDS) image (Figure S8) and XRD pattern (Figure S5). The even elemental distribution of sodium, carbon, oxygen, and nickel inside the pyrolysis product is shown in the EDS mapping (Figure 1E–I). The catalytic effect of nickel nanoparticles embedded in the carbon skeleton makes the graphene layers grow around the nickel particles, which subsequently forms a nanocage morphology with sizes from several dozen to several hundred nanometers (Figure 1J). The interconnected nanocage morphology is also confirmed by the TEM image in Figure 1K. The graphitic structure of GCNC is confirmed by HRTEM (Figure 1L), with a (002) lattice spacing of 0.345 nm.

The crystal structures of HAPC and GCNC carbons were analyzed using XRD. Figure 2A shows that GCNC has a well-defined (002) peak at 26.2° , corresponding to an interlayer spacing of 0.340 nm, which is consistent with the HRTEM result. The (002) peak of HAPC is located in a broad range of 2θ , which demonstrates that HAPC is amorphous, without a well-defined interlayer spacing. Raman spectroscopy was then used to characterize the structure of GCNC and HPAC. Figure 2B shows that GCNC exhibits four typical bands, including the G band around 1580 cm^{-1} from graphitic carbon, the D band around 1350 cm^{-1} , the D' band around 1620 cm^{-1} induced by defects, and the 2D band around 2700 cm^{-1} . The appearance of a 2D peak is a sign of multilayer stacking of graphene. The

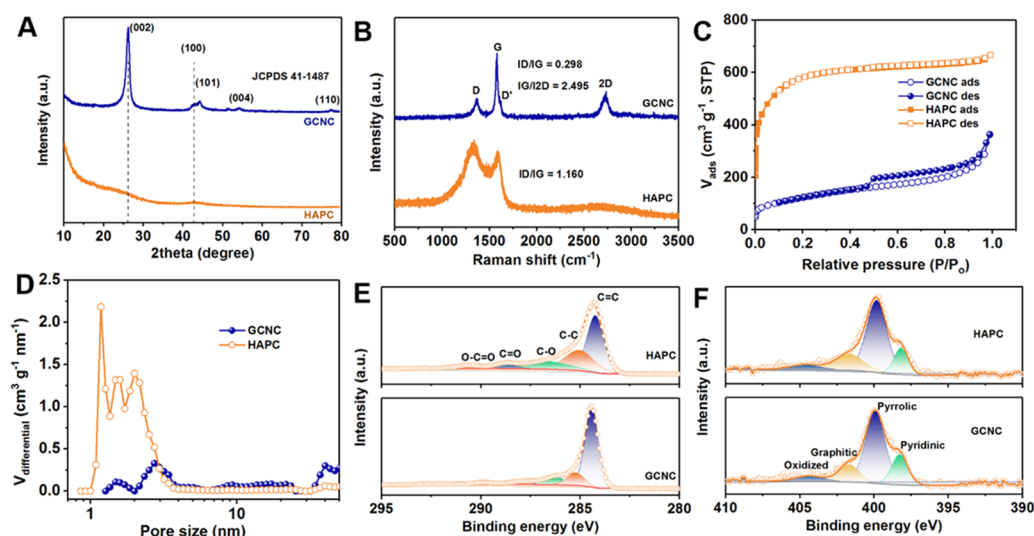


Figure 2. Physicochemical characterizations of GCNC and HAPC. (A) XRD patterns, (B) Raman spectra, (C) nitrogen adsorption/desorption isotherms, (D) pore size distribution curves, (E) C 1s fine spectra with fitting results, and (F) N 1s fine spectra with fitting results.

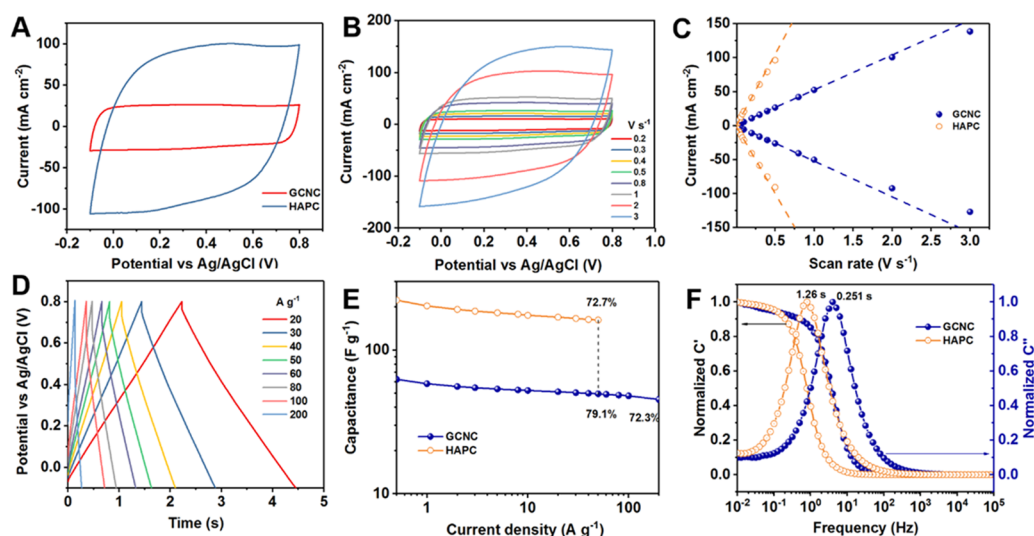


Figure 3. Electrochemical performances of GCNC and HAPC electrodes. (A) Cyclic voltammograms of GCNC and HAPC at 0.5 V s^{-1} , (B) cyclic voltammograms of GCNC at different scan rates, (C) dependence of current responses of cyclic voltammograms on scan rate, (D) GCD curves of GCNC at different current densities, (E) dependence of the gravimetric capacitances on the current densities, and (F) dependence of the normalized real and imaginary capacitances on the frequency.

I_D/I_G ratio of GCNC is 0.298, indicative of the existence of defects in GCNC. In contrast, HAPC shows an I_D/I_G ratio of 1.16 and lacks the 2D band, which is due to the amorphous nature of HAPC and consistent with the XRD and TEM results. The I_G/I_{2D} ratio of GCNC is 2.495, which is a sign that GCNC is a carbonaceous material with multilayered graphene.³⁵ The graphitic nature of GCNC endows it with high conductivity, which is good for achieving high rate performance in supercapacitors. SSA and pore size distribution (PSD) are important parameters to evaluate the capacitances of carbon materials.⁶⁴ Therefore, the N_2 adsorption/desorption method was used to characterize the SSA and PSD of GCNC and HAPC. The SSAs were calculated using the Brunauer–Emmett–Teller (BET) model, and the PSDs were calculated using nonlocal density functional theory. The nitrogen adsorption of HAPC shows a type I isotherm, while GCNC shows a type IV isotherm (Figure 2C), according to the classification of the International Union of Pure and

Applied Chemistry. These results indicate that HAPC is a micropore-dominated electrode while GCNC is mesopore-dominated. The BET SSA of HAPC is $2127.2 \text{ m}^2 \text{ g}^{-1}$ with a total pore volume of $1.031 \text{ cm}^3 \text{ g}^{-1}$, while the BET SSA of GCNC is $438.7 \text{ m}^2 \text{ g}^{-1}$ with a total pore volume of $0.562 \text{ cm}^3 \text{ g}^{-1}$. The much lower BET SSA of GCNC compared to HAPC derived from EDTA disodium salt could be due to the catalytic effect of nickel metal on graphitization in the case of the GCNC precursor, where most carbon atoms grow on the nickel metal and do not react with Na_2CO_3 to form pores. There are three peaks located at 1.18, 1.32, and 2.00 nm , in the PSD graph (Figure 2D) of HAPC. The average pore size of HAPC is estimated to be around 1.94 nm (Table S1). In comparison, the PSD of GCNC has three peaks located at 1.483, 2.734, and 40.0 nm , with an average pore size of 5.12 nm . Most of the pores of GCNC are located in the mesopore range. Some mesopores are larger than 30 nm , which is due to the template effect of nickel particles. The larger pore size and

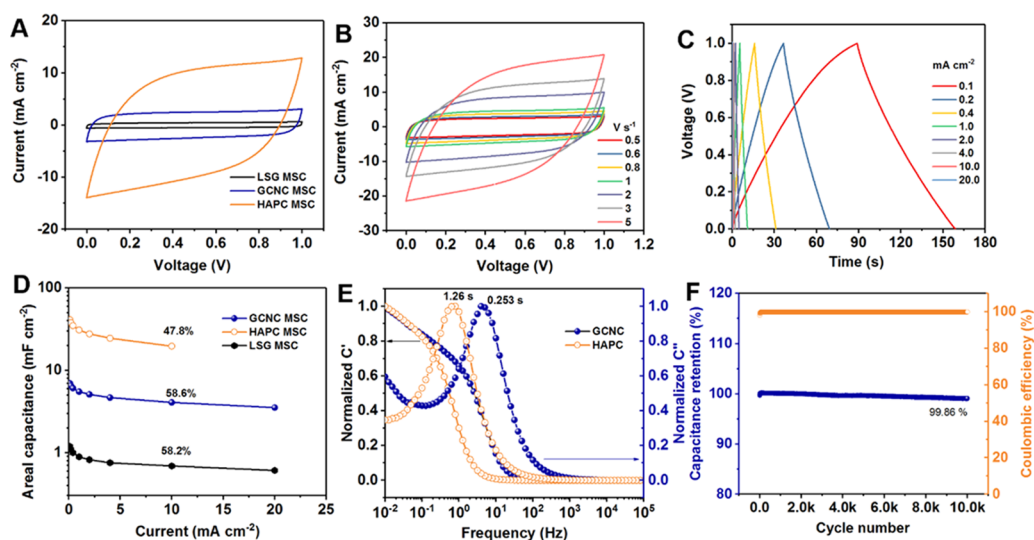


Figure 4. Electrochemical performances of GCNC and HAPC MSCs fabricated using the WDA process. (A) Cyclic voltammograms of MSCs at a scan rate of 0.5 V s^{-1} , (B) cyclic voltammograms of GCNC MSC at different scan rates, (C) GCD curves of GCNC, HAPC, and LSG MSCs at different current densities, (D) dependence of the areal capacitances of GCNC, HAPC, and LSG MSCs on current densities, (E) dependence of the normalized real and imaginary capacitances of MSCs on the frequency, and (F) GCD cycling performance of HAPC MSC at a current density of 10 mA cm^{-2} .

lower SSA of GCNC compared to HAPC could make it a high-rate-performance electrode, but at the cost of low specific capacitance. Compared to the pore structure of HAPC derived from EDTA disodium, it can be seen that the pore size and crystal structure of GCNC and HAPC can be controlled well by modifying the chemical structure of EDTA-based salts. Next, the chemical compositions of GCNC and HAPC were studied by X-ray photoelectron spectroscopy (XPS). GCNC and HAPC both contain about 3 atom % nitrogen (Figure S9), which could improve the pseudocapacitance of HAPC and GCNC. On the other hand, GCNC contains less oxygen than HAPC does, as shown in Figure S9, which could be due to its smaller SSA. The C 1s and N 1s fine spectra were fitted to study the chemical bonding in GCNC and HAPC (Figure 2E,F). As shown in Table S2, the C 1s spectra can be fitted into 5 components as follows: $\text{sp}^2 \text{ C}=\text{C}$ located at 284.4 eV, $\text{sp}^3 \text{ C}-\text{C}$ located at 285.0 eV, C-O ($\text{sp}^2 \text{ C}-\text{N}$ included) located at 286.6 eV, C=O ($\text{sp}^3 \text{ C}-\text{N}$) located at 288.7 eV, and O-C=O located at 290.6 eV. GCNC contains a much higher $\text{sp}^2 \text{ C}=\text{C}$ (68.12 atom %) than HAPC does (46.57 atom %). The nitrogen bonding is fitted by four components (Table S3): pyridinic N located at 398.0 eV, pyrrolic N located at 399.7 eV, graphitic N located at 401.7 eV, and oxidized N located at 404.5 eV. Both HAPC and GCNC have high edge-nitrogen-bonding of pyridinic N and pyrrolic N, which could contribute to pseudocapacitance.

The above results clearly show that by tuning the chemical structure of EDTA-based salt, two kinds of porous carbon electrode materials are obtained (HAPC and GCNC), which have different crystal structures, pore structures, and surface chemical compositions. Using these two porous carbons as active materials in MSCs, we can tune the electrochemical performance of the MSCs.

The electrochemical performances of HAPC and GCNC were studied using cyclic voltammetry, galvanostatic charge-discharge (GCD), and electrochemical impedance in a three-electrode setup. Figure 3A shows the cyclic voltammograms of HAPC and GCNC, which indicates that HAPC has a higher

capacitance than GCNC. The smaller hysteresis of the cyclic voltammogram of GCNC compared to that of HAPC indicates smaller impedance. As a result of high SSA, HAPC has a higher capacitance, while GCNC has a higher rate capability ascribed to its higher conductivity and larger pore size. GCNC can be scanned from 0.01 (Figure S10A) to as high as 3 V s^{-1} (Figure 3B), which indicates that GCNC can be charged/discharged within 0.3 s. The HAPC electrode can only be scanned by up to 0.5 V s^{-1} (Figure S11A). Furthermore, the current response of GCNC has an almost linear relationship, with a scan rate up to 2 V s^{-1} , while the current response of HAPC has a linear relationship with a scan rate up to 0.3 V s^{-1} only (Figure 3C). This result demonstrates the excellent rate performance and quasi-ideal capacitive behavior of GCNC. With its excellent rate performance, GCNC can be charged/discharged over a wide current range from 0.5 (Figure S10B) to 200 A g^{-1} (Figure 3D). GCNC has one of the best rate performances in the porous carbon electrode family.^{65,66} In contrast, HAPC can only be charged/discharged in the current range from 0.5 to 50 A g^{-1} (Figure S11B). Based on calculation from the GCD curves, HAPC has a high specific capacitance of 223 F g^{-1} , while GCNC has a specific capacitance of only 62.7 F g^{-1} at 0.5 A g^{-1} (Figure 3E). At 50 A g^{-1} , the capacitance retention of HAPC is 72.7%, while the capacitance retention of GCNC is 79.1%. On increasing the current density up to 200 A g^{-1} , the GCNC exhibits a high capacitance retention of 72.3%. The excellent rate performance of GCNC originates from the high conductivity of its graphitic structure and the short diffusion path resulting from its meso/macropore-dominated structure. The high conductivity and short diffusion path endow GCNC with low impedance (Nyquist plots are shown in Figure S12) and high frequency response (Figure 3F). GCNC has a small time constant of 0.251 s, while HAPC has a relatively high time constant of 1.26 s, comparable to other porous carbon materials.⁶⁷

WDA is demonstrated to be a promising technique for the assembly of MSC. After the WDA process, not only the finger electrodes are separated, but also the LSG surface is uniformly

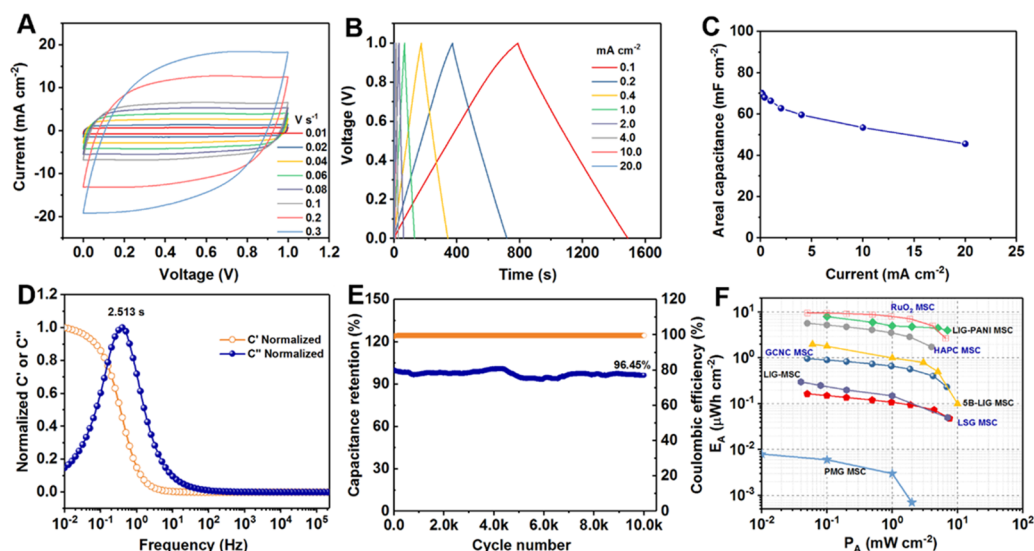


Figure 5. Electrochemical performances of RuO₂ MSCs fabricated using the WDA process. (A) Cyclic voltammograms at different scan rates, (B) GCD curves at different current densities, (C) dependence of areal capacitance on current densities, (D) dependence of the normalized real and imaginary capacitances on frequency, (E) GCD cycling performance of RuO₂ MSC at a current density of 10 mA cm⁻², and (F) comparison of the Ragone plot of the MSC with other MSCs from the literature (detailed data are shown in Table S4).

covered by HAPC and GCNC (Figure S13). The electrochemical performances of HAPC and GCNC MSCs fabricated using the water-based WDA process are plotted in Figure 4. LSG itself can be used as a binder-free electrode for MSCs. Although LSG-based MSCs can be scanned up to 20 V s⁻¹ (Figure S14) and displays a very low time constant of 20 ms, LSG has limited capacitance (1.2 mF cm⁻² at 0.1 mA cm⁻²). Nevertheless, the low internal resistance of LSG MSC (Figure S14D,E) indicates that it can be used as a 3D current collector for MSC. By assembling MSCs using the WDA process, with HAPC or GCNC as active materials, the electrochemical performance of MSCs can be greatly improved. The GCNC and HAPC MSCs both have much higher capacitances than LSG-only MSCs, as can be seen from the cyclic voltammograms in Figure 4A. The GCNC MSCs can be scanned from 0.01 (Figure S15) to as high as 5 V s⁻¹ (Figure 4B), which means that they can be charged/discharged within 0.2 s. In contrast, HAPC MSCs can be scanned only up to 0.8 V s⁻¹ (Figure S16A). Furthermore, the GCNC MSCs exhibit triangular GCD curves from 0.1 to 20 mA cm⁻² (Figure 4C), while the HAPC MSCs show a triangular GCD shape up to 10 mA cm⁻² (Figure S16B). The HAPC MSC shows an asymmetric GCD curve at 0.1 mA cm⁻² due to the side reactions at the end of charge. The HAPC MSCs have a high capacitance due to the micro/mesopore-dominated, highly porous structure of HAPC, while GCNC MSCs have a moderate capacitance due to the limited SSA. However, both GCNC and HAPC MSCs have a higher capacitance than LSG-only MSC. Furthermore, the HAPC MSC exhibits an areal capacitance of 41.17 mF cm⁻², while GCNC MSC exhibits a capacitance of 6.97 mF cm⁻² at the current density of 0.1 mA cm⁻². On increasing the current density to 10 mA cm⁻², the capacitance retention is 47.8 and 58.6% for the HAPC and GCNC MSC, respectively (Figure 4D). Both the HAPC and GCNC MSCs show slightly higher equivalent series resistance than LSG-only MSCs do (Figure S17), indicating excellent contact between porous carbon and LSG current collectors. Moreover, the HAPC and GCNC MSC devices exhibit time constants of 1.26 and 0.23 s, respectively (Figure 4E). These

values are comparable to the values measured in a three-electrode configuration using HAPC and GCNC electrodes, suggesting that there is no degradation in electrode performance as a result of the WDA process. Finally, the HAPC and GCNC MSC devices show high stability with a capacitance retention higher than 99% after 10 000 GCD cycles (Figures 4F and S18). All in all, the greatly improved capacitance and excellent charge–discharge behaviors of HAPC and GCNC MSC devices indicate the viability and robustness of our WDA process.

Next, we demonstrate that our WDA process is universal and can be used to assemble MSCs using other pseudocapacitive electrode materials, besides porous carbons. We synthesized RuO₂ slurries and used the WDA process to fabricate pseudocapacitive MSCs. RuO₂ was chosen because it is a well-known pseudocapacitive material with high capacitance and stable electrochemical performance. Although the price of RuO₂ is high compared to other transition-metal oxides, the cost of MSC should not increase too much since MSC use limited mass loading of RuO₂. The highly stable cycling performance of RuO₂ compensates for the high cost of RuO₂. The hydrothermally synthesized RuO₂ particles are amorphous (Figure S19) and have spherical morphology (Figure S20). First, we characterized the RuO₂ electrode material in three-electrode measurements. The RuO₂ electrodes show capacitive behavior in the potential range of 0–1 V (Figure S21A). Furthermore, they exhibit high capacitance under current density of 1–50 A g⁻¹ (Figure S21B). Specifically, RuO₂ exhibits capacitances of 432.2 and 361.5 F g⁻¹ at 1 and 50 A g⁻¹, respectively (Figure S21C).

To fabricate MSC devices using RuO₂, we prepared water-based slurries and coated LSG-patterned substrates with them using our WDA process (Figure S22). The RuO₂ MSCs prepared using the WDA process exhibit rectangular-shaped CV curves from 0.01 to 0.3 V s⁻¹ (Figure 5A), indicating the quasi-ideal capacitive behavior of these MSCs. Furthermore, the GCD curves of RuO₂ MSCs also have triangular shapes, indicating their quasi-ideal capacitive behavior (Figure 5B). The capacitance of RuO₂ MSCs is 70.33 mF cm⁻² at 0.1 mA

cm^{-2} . At a high current density of 20 mA cm^{-2} , the areal capacitance of RuO_2 MSCs is still as high as 45.63 mF cm^{-2} (Figure 5C). Due to the slow pseudocapacitive energy storage kinetics, RuO_2 MSCs exhibit a time constant of 2.51 s (Figure 5D), which is longer than that for MSC devices fabricated using HAPC and GCNC. Furthermore, RuO_2 MSCs demonstrate excellent cycling stability: a high capacitance retention of 96.55% is achieved after 10 000 GCD cycles (Figure 5E). The RuO_2 particles are firmly embedded in the 3D structure of LSG (Figure S23) after 10 000 GCD cycles, demonstrating its superior stability during cycling.

With the realization of RuO_2 MSCs, we can conclude that the WDA process is a general process for the assembly of MSCs using slurries of various active materials. The assembled HAPC, GCNC, and RuO_2 MSCs show high capacitance and high rate performance, leading to high areal energy power densities (data compared in Ragone plot in Figure 5F). The GCNC-based MSCs exhibit an areal energy density of $0.968 \mu\text{Wh cm}^{-2}$, which is 6 times higher than that of LSG-only MSCs. Furthermore, the GCNC-based MSCs show a high areal power density of 6.88 mW cm^{-2} . In comparison, the HAPC-based MSCs exhibit a high areal energy of $5.71 \mu\text{Wh cm}^{-2}$, with a maximum power density of 4.0 mW cm^{-2} . The energy and power characteristics of MSCs are further enhanced by applying the WDA process to RuO_2 . The energy density of the RuO_2 -based MSCs is $9.71 \mu\text{Wh cm}^{-2}$. The properties of the WDA-assembled MSCs are compared with the literature data (Table S4), revealing that the capacitance and energy density of the HAPC-based MSCs outperform most recently reported carbon-based MSCs with a high-level areal power density.

3. CONCLUSIONS

In summary, we have designed a WDA process for the fabrication of electrochemical MSCs. The WDA process takes advantage of the different wetting behavior of LSG and polyimide toward water. With a simple slurry coating and drying process, various supercapacitor electrode materials (porous carbon and RuO_2) are selectively assembled on the surface of patterned 3D LSG. The WDA process enables the fabrication of MSCs with high capacitance compared to other carbon-based MSCs. Since the WDA process only uses water as a solvent and drying technique, it is considered to be a green process. With these features, WDA is greener, faster, and simpler than other MSC fabrication techniques such as electrodeposition, screen printing, electrophoretic deposition, and photolithography. Furthermore, WDA is a versatile technique and can be extended to other electrode materials, such as conductive polymers, metal hydroxides, sulfides, and nitrides, paving the way for a new and simple fabrication methodology of electrochemical MSCs.

4. EXPERIMENTAL SECTION

4.1. Preparation of Active Materials. GCNC and HAPC were prepared from direct pyrolysis of organic compounds based on EDTA disodium salt dihydrate. First, 37.2 g of EDTA disodium salt dihydrate was mixed with 8 g of NaOH in 200 mL of deionized water under stirring at 80°C for 24 h and then dried at 80°C to form EDTA tetrasodium salt powders. Furthermore, 37.2 g of EDTA disodium salt dihydrate was mixed with 24.88 g of nickel acetate hexahydrate in 200 mL of deionized water under stirring at 80°C for 24 h and then dried at 100°C for 2 days to obtain nickel EDTA nickel coordination salt. HAPC and GCNC were obtained by pyrolysis of EDTA tetrasodium salt and EDTA nickel coordination

compound, respectively, in a nickel crucible at 700°C for 1 h with a ramping rate of 2°C min^{-1} in argon atmosphere. The obtained pyrolysis products were washed with superfluous $10 \text{ wt } \% \text{ HCl}$ at 80°C for 24 h to remove impurities inside the carbon skeleton. The final porous carbon materials were obtained after washing, by vacuum filtering and dried in an 80°C vacuum oven overnight. RuO_2 nanoparticles were prepared using the hydrothermal method. $\text{RuCl}_3 \cdot x\text{H}_2\text{O}$ (0.6 g) was dissolved in 40 mL of deionized water and sealed in a 50 mL hydrothermal reactor in an airflow oven at 180°C for 20 h . After the hydrothermal reaction, the product was centrifuged with water at least five times and dried in an oven at 150°C for 1 h .

4.2. WDA Process of the MSC. The 3D LSG patterns were used as the current collector in this work. LSGs were prepared from direct laser writing of a commercial Kapton polyimide film with a 75 W CO_2 laser cutting machine (Universal X-660 laser cutter platform, Universal, Austria) in air. The laser power used in this work was 4.5% . Other typical settings were the same as in our previous publication.⁴⁰ After laser scribing, the LSGs were directly used as the current collector of the MSC without further modification.

The GCNC, HAPC, and RuO_2 particles were ground manually for 30 min to achieve particulate with small size around $1 \mu\text{m}$. Before the assembly of the MSC, 40 mg of GCNC, HAPC, or RuO_2 powders (80%) were mixed with 10% sodium carboxymethyl cellulose (CMC) binders (1.0% in deionized water solvent) and 10% acetylene black to form a homogeneous slurry. The total amount of liquid in the slurry was controlled to be 2 mL (concentration, 20 mg mL^{-1}). The fabrication of a WDA-enabled MSC was as follows. The LSG patterns were well attached to a flat glass substrate, and then the whole surface of the finger electrodes and the gaps between them were coated with the porous carbon slurry ($40 \mu\text{L}$). Then, the LSG patterns were put in a 70°C vacuum oven for at least 1 h . After that, the MSC with the finger electrodes coated with particulate active materials was obtained. Before electrochemical measurement, the MSC was connected to copper tape using silver paint (Ted Pella Inc.). To separate the electrolyte and silver paint, the space between the finger electrodes and the silver paint was coated with epoxy resin. Subsequently, $1 \text{ M H}_2\text{SO}_4/\text{PVA}$ gel electrolyte was pasted onto the finger electrodes and left in the air for at least 4 h to ensure the full saturation of the gel electrolyte in the pores of active materials. The preparation of $\text{H}_2\text{SO}_4/\text{PVA}$ gel electrolyte was the same as in our previous publication.⁴⁰

4.3. Physicochemical Characterization. A N_2 adsorption/desorption analyzer (ASAP 2420, Micromeritics) was used to collect the adsorption and desorption isotherms. The Brunauer–Emmett–Teller (BET) model was used to evaluate the specific surface area, and nonlocal density functional theory was employed to simulate the pore size distribution. Scanning electron microscopy (SEM) images were collected on a scanning electron microscope (Merlin, ZEISS, Germany). Furthermore, a transmission electron microscope (Titan 80-300 ST, FEI, Thermo Fisher Scientific) was used to obtain the TEM images. X-ray diffraction (XRD) patterns were collected on an X-ray diffractometer (D8 Advance, Bruker, Germany) with $\text{Cu K}\alpha$ radiation ($\lambda = 1.5406 \text{ \AA}$), while Raman spectra were obtained on a micro-Raman spectrometer (LabRAM ARAMIS, Horiba-Jobin Yvon, Germany) using a cobalt laser (473 nm) with a 1% filter. Finally, X-ray photoelectron spectroscopy (XPS) analysis was conducted on a photoelectron spectrometer (Kratos AXIS Supra, Shimadzu, Japan).

4.4. Electrochemical Characterization and Calculation. For the three-electrode measurement, 80% active materials (GCNC, HAPC, or RuO_2) were mixed with 10% poly(vinylidene difluoride) binder ($5 \text{ wt } \% \text{ in NMP solvent}$) and 10% acetylene black to form a homogeneous slurry. The well-mixed slurry was drop-cast onto carbon paper serving as the working electrode (mass loading of ca. 2 mg cm^{-2}). After drying in an 80°C vacuum oven overnight, the mass loading was calculated using the difference heavy method. The test of three electrodes in an electrolytic cell was carried out using Ag/AgCl as the reference electrode and a platinum wire as the counter electrode in $1 \text{ M H}_2\text{SO}_4$ aqueous electrolyte.

All of the electrochemical tests were performed on an electrochemical workstation (VMP3, Biologic, France). Cyclic voltammetry (CV), galvanostatic charge–discharge (GCD), and electrochemical

impedance tests were used to evaluate the electrochemical performance of single active material using the three-electrode method, or the electrochemical performances of MSC using the two-electrode method. The electrochemical impedance spectrum was measured at open-circuit voltage in the frequency range of 200 kHz to 10 mHz with a sinusoidal voltage amplitude of 10 mV. All of the measurements were conducted in ambient conditions.

The specific gravimetric capacitances of GCNC, HAPC, and RuO₂ were calculated from the discharge portion of GCD curves using eq 1.

$$C_g = \frac{I\Delta t}{m\Delta V} \quad (1)$$

The areal capacitances of MSC were calculated from the discharge portion of GCD curves using eq 2.

$$C_A = \frac{I\Delta t}{S\Delta V} \quad (2)$$

In eqs 1 and 2, I is the constant current in GCD measurements, ΔV is the voltage change during the discharge process, which was calculated using the maximum voltage upon charge minus the voltage drop during initial discharge, Δt is the discharge time in seconds, S is the area of MSC in cm², and m is the mass of active materials.

Areal energy densities (E_A) and power densities (P_A) were calculated to evaluate energy storage capability of one unit area using the following eqs 3 and 4.

$$E_A = \frac{1}{2} \times \frac{C_A V^2}{3600} \quad (3)$$

$$P_A = \frac{3600 \times E_A}{\Delta t} \quad (4)$$

where C_A is the areal capacitance in GCD measurement (in mF cm⁻²), V is the voltage window (V) with the subtraction of the voltage drop at the beginning of discharge, and Δt is the discharge time in seconds.

The imaginary and real capacitances were calculated to evaluate the capacitance response and the time constant according to eqs 5 and 6.

$$C' = \frac{-Z''}{2\pi f A |Z|^2} \quad (5)$$

$$C'' = \frac{Z'}{2\pi f A |Z|^2} \quad (6)$$

RC time constant was calculated using eq 7, where f_0 is the frequency at which the imaginary capacitance reaches the maximum.

$$\tau = \frac{1}{f_0} \quad (7)$$

■ ASSOCIATED CONTENT

Supporting Information

The Supporting Information is available free of charge on the ACS Publications website at DOI: 10.1021/acsami.9b05635.

Physicochemical characterizations of HAPC, GCNC, and LSG; three-electrode electrochemical characterizations of HAPC, GCNC, and RuO₂ nanoparticles; and the performance comparison of MSCs fabricated using WDA and MSCs from the literature (PDF)

■ AUTHOR INFORMATION

Corresponding Author

*E-mail: husam.alshareef@kaust.edu.sa.

ORCID

Wenli Zhang: 0000-0002-6781-2826

Husam N. Alshareef: 0000-0001-5029-2142

Notes

The authors declare no competing financial interest.

■ ACKNOWLEDGMENTS

The research reported in this publication was supported by King Abdullah University of Science and Technology (KAUST). The authors acknowledge the Advanced Nanofabrication, Imaging and Characterization and Analytical Chemistry Core Laboratories at KAUST for the support.

■ REFERENCES

- (1) Kyeremateng, N. A.; Brousse, T.; Pech, D. Microsupercapacitors as Miniaturized Energy-Storage Components for on-Chip Electronics. *Nat. Nanotechnol.* **2017**, *12*, 7–15.
- (2) Qi, D.; Liu, Y.; Liu, Z.; Zhang, L.; Chen, X. Design of Architectures and Materials in In-Plane Micro-Supercapacitors: Current Status and Future Challenges. *Adv. Mater.* **2017**, *29*, No. 1602802.
- (3) Da, Y.; Liu, J.; Zhou, L.; Zhu, X.; Chen, X.; Fu, L. Engineering 2D Architectures toward High-Performance Micro-Supercapacitors. *Adv. Mater.* **2018**, *30*, No. 1802793.
- (4) He, B.; Zhang, Q.; Li, L.; Sun, J.; Man, P.; Zhou, Z.; Li, Q.; Guo, J.; Xie, L.; Li, C.; et al. High-Performance Flexible All-Solid-State Aqueous Rechargeable Zn-MnO₂ Microbatteries Integrated with Wearable Pressure Sensors. *J. Mater. Chem. A* **2018**, *6*, 14594–14601.
- (5) Beidaghi, M.; Gogotsi, Y. Capacitive Energy Storage in Micro-Scale Devices: Recent Advances in Design and Fabrication of Micro-Supercapacitors. *Energy Environ. Sci.* **2014**, *7*, 867–884.
- (6) Chmiola, J.; Largeot, C.; Taberna, P.-L.; Simon, P.; Gogotsi, Y. Monolithic Carbide-Derived Carbon Films for Micro-Supercapacitor. *Science* **2010**, *328*, 480–483.
- (7) Huang, P.; Lethien, C.; Pinaud, S.; Brousse, K.; Laloo, R.; Turq, V.; Respaud, M.; Demortière, A.; Daffos, B.; Taberna, P. L.; et al. On-Chip and Freestanding Elastic Carbon Films for Micro-Supercapacitors. *Science* **2016**, *351*, 691–695.
- (8) Zhuang, X.; Feng, X. Silicon-Compatible Carbon-Based Micro-Supercapacitors. *Angew. Chem., Int. Ed.* **2016**, *55*, 6136–6138.
- (9) Miller, J. R. Valuing Reversible Energy Storage. *Science* **2012**, *335*, 1312–1313.
- (10) Peng, Y. Y.; Akuzum, B.; Kurra, N.; Zhao, M. Q.; Alhabeab, M.; Anasori, B.; Kumbur, E. C.; Alshareef, H. N.; Ger, M.-D.; Gogotsi, Y. All-MXene (2D Titanium Carbide) Solid-State Microsupercapacitors for on-Chip Energy Storage. *Energy Environ. Sci.* **2016**, *9*, 2847–2854.
- (11) Zhang, C. J.; Kremer, M. P.; Seral-Ascaso, A.; Park, S. H.; McEvoy, N.; Anasori, B.; Gogotsi, Y.; Nicolosi, V. Stamping of Flexible, Coplanar Micro-Supercapacitors Using MXene Inks. *Adv. Funct. Mater.* **2018**, *28*, No. 1705506.
- (12) Zhang, C.; McKeon, L.; Kremer, M. P.; Park, S.-H.; Ronan, O.; Seral-Ascaso, A.; Barwich, S.; Coileáin, C. O.; McEvoy, N.; Nerl, H. C.; et al. Additive-Free MXene Inks and Direct Printing of Micro-Supercapacitors. *Nat. Commun.* **2019**, *10*, No. 1795.
- (13) Zhang, Q.; Zhang, J.; Zhou, Z.; Wei, L.; Yao, Y. Flexible Quasi-Solid-State 2.4 V Aqueous Asymmetric Microsupercapacitors with Ultrahigh Energy Density. *J. Mater. Chem. A* **2018**, *6*, 20145–20151.
- (14) Kurra, N.; Ahmed, B.; Gogotsi, Y.; Alshareef, H. N. MXene-on-Paper Coplanar Microsupercapacitors. *Adv. Energy Mater.* **2016**, *6*, No. 1601372.
- (15) Li, Y. Q.; Shi, X. M.; Lang, X. Y.; Wen, Z.; Li, J. C.; Jiang, Q. Remarkable Improvements in Volumetric Energy and Power of 3D MnO₂ Microsupercapacitors by Tuning Crystallographic Structures. *Adv. Funct. Mater.* **2016**, *26*, 1830–1839.
- (16) Jiang, Q.; Kurra, N.; Xia, C.; Alshareef, H. N. Hybrid Microsupercapacitors with Vertically Scaled 3D Current Collectors Fabricated Using a Simple Cut-and-Transfer Strategy. *Adv. Energy Mater.* **2017**, *7*, No. 1601257.
- (17) Jiang, Q.; Kurra, N.; Alhabeab, M.; Gogotsi, Y.; Alshareef, H. N. All Pseudocapacitive MXene-RuO₂ Asymmetric Supercapacitors. *Adv. Energy Mater.* **2018**, *8*, No. 1703043.

- (18) Ferris, A.; Garbarino, S.; Guay, D.; Pech, D. 3D RuO₂ Microsupercapacitors with Remarkable Areal Energy. *Adv. Mater.* **2015**, *27*, 6625–6629.
- (19) El-Kady, M. F.; Ihns, M.; Li, M.; Hwang, J. Y.; Mousavi, M. F.; Chaney, L.; Lech, A. T.; Kaner, R. B. Engineering Three-Dimensional Hybrid Supercapacitors and Microsupercapacitors for High-Performance Integrated Energy Storage. *Proc. Natl. Acad. Sci. U.S.A.* **2015**, *112*, 4233–4238.
- (20) Cao, L.; Yang, S.; Gao, W.; Liu, Z.; Gong, Y.; Ma, L.; Shi, G.; Lei, S.; Zhang, Y.; Zhang, S.; et al. Direct Laser-Patterned Micro-Supercapacitors from Paintable MoS₂ Films. *Small* **2013**, *9*, 2905–2910.
- (21) Li, L.; Zhang, J.; Peng, Z.; Li, Y.; Gao, C.; Ji, Y.; Ye, R.; Kim, N. D.; Zhong, Q.; Yang, Y.; et al. High-Performance Pseudocapacitive Microsupercapacitors from Laser-Induced Graphene. *Adv. Mater.* **2016**, *28*, 838–845.
- (22) Kurra, N.; Jiang, Q.; Syed, A.; Xia, C.; Alshareef, H. N. Micro-Pseudocapacitors with Electroactive Polymer Electrodes: Toward AC-Line Filtering Applications. *ACS Appl. Mater. Interfaces* **2016**, *8*, 12748–12755.
- (23) Hwang, J. Y.; Li, M.; El-Kady, M. F.; Kaner, R. B. Next-Generation Activated Carbon Supercapacitors: A Simple Step in Electrode Processing Leads to Remarkable Gains in Energy Density. *Adv. Funct. Mater.* **2017**, *27*, No. 1605745.
- (24) Yao, L.; Wu, Q.; Zhang, P.; Zhang, J.; Wang, D.; Li, Y.; Ren, X.; Mi, H.; Deng, L.; Zheng, Z. Scalable 2D Hierarchical Porous Carbon Nanosheets for Flexible Supercapacitors with Ultrahigh Energy Density. *Adv. Mater.* **2018**, *30*, No. 1706054.
- (25) Li, L.; Secor, E. B.; Chen, K. S.; Zhu, J.; Liu, X.; Gao, T. Z.; Seo, J. W. T.; Zhao, Y.; Hersam, M. C. High-Performance Solid-State Supercapacitors and Microsupercapacitors Derived from Printable Graphene Inks. *Adv. Energy Mater.* **2016**, *6*, No. 1600909.
- (26) Liu, Z.; Wu, Z. S.; Yang, S.; Dong, R.; Feng, X.; Müllen, K. Ultraflexible In-Plane Micro-Supercapacitors by Direct Printing of Solution-Processable Electrochemically Exfoliated Graphene. *Adv. Mater.* **2016**, *28*, 2217–2222.
- (27) Pech, D.; Brunet, M.; Durou, H.; Huang, P.; Mochalin, V.; Gogotsi, Y.; Taberna, P.-L.; Simon, P. Ultrahigh-Power Micrometre-Sized Supercapacitors Based on Onion-like Carbon. *Nat. Nanotechnol.* **2010**, *5*, 651–654.
- (28) Niu, Z.; Zhang, L.; Liu, L.; Zhu, B.; Dong, H.; Chen, X. All-Solid-State Flexible Ultrathin Micro-Supercapacitors Based on Graphene. *Adv. Mater.* **2013**, *25*, 4035–4042.
- (29) Zhu, M.; Huang, Y.; Huang, Y.; Li, H.; Wang, Z.; Pei, Z.; Xue, Q.; Geng, H.; Zhi, C. A Highly Durable, Transferable, and Substrate-Versatile High-Performance All-Polymer Micro-Supercapacitor with Plug-and-Play Function. *Adv. Mater.* **2017**, *29*, No. 1605137.
- (30) Li, L.; Fu, C.; Lou, Z.; Chen, S.; Han, W.; Jiang, K.; Chen, D.; Shen, G. Flexible Planar Concentric Circular Micro-Supercapacitor Arrays for Wearable Gas Sensing Application. *Nano Energy* **2017**, *41*, 261–268.
- (31) Ye, R.; James, D. K.; Tour, J. M. Laser-Induced Graphene: From Discovery to Translation. *Adv. Mater.* **2019**, *31*, No. 1803621.
- (32) Ye, R.; James, D. K.; Tour, J. M. Laser-Induced Graphene. *Acc. Chem. Res.* **2018**, *51*, 1609–1620.
- (33) Zhang, W.; Lei, Y.; Jiang, Q.; Ming, F.; Costa, P. M. F. J.; Alshareef, H. N. 3D Laser Scribed Graphene Derived from Carbon Nanospheres: An Ultrahigh-Power Electrode for Supercapacitors. *Small Methods* **2019**, *3*, No. 1900005.
- (34) Lamberti, A.; Clerici, F.; Fontana, M.; Scaltrito, L. A Highly Stretchable Supercapacitor Using Laser-Induced Graphene Electrodes onto Elastomeric Substrate. *Adv. Energy Mater.* **2016**, *6*, No. 1600050.
- (35) Lin, J.; Peng, Z.; Liu, Y.; Ruiz-Zepeda, F.; Ye, R.; Samuel, E. L. G.; Yacaman, M. J.; Jakobson, B. I.; Tour, J. M. Laser-Induced Porous Graphene Films from Commercial Polymers. *Nat. Commun.* **2014**, *5*, No. 5714.
- (36) Li, Y.; Luong, D. X.; Zhang, J.; Tarkunde, Y. R.; Kittrell, C.; Sargunara, F.; Ji, Y.; Arnusch, C. J.; Tour, J. M. Laser-Induced Graphene in Controlled Atmospheres: From Superhydrophilic to Superhydrophobic Surfaces. *Adv. Mater.* **2017**, *29*, No. 1700496.
- (37) El-Kady, M. F.; Strong, V.; Dubin, S.; Kaner, R. B. Laser Scribing of High-Performance and Flexible Graphene-Based Electrochemical Capacitors. *Science* **2012**, *335*, 1326–1330.
- (38) Gao, W.; Singh, N.; Song, L.; Liu, Z.; Reddy, A. L. M.; Ci, L.; Vajtai, R.; Zhang, Q.; Wei, B.; Ajayan, P. M. Direct Laser Writing of Micro-Supercapacitors on Hydrated Graphite Oxide Films. *Nat. Nanotechnol.* **2011**, *6*, 496–500.
- (39) El-Kady, M. F.; Kaner, R. B. Scalable Fabrication of High-Power Graphene Micro-Supercapacitors for Flexible and on-Chip Energy Storage. *Nat. Commun.* **2013**, *4*, No. 1475.
- (40) Zhang, W.; Lei, Y.; Ming, F.; Jiang, Q.; Costa, P. M. F. J.; Alshareef, H. N. Lignin Laser Lithography: A Direct-Write Method for Fabricating 3D Graphene Electrodes for Microsupercapacitors. *Adv. Energy Mater.* **2018**, *8*, No. 1801840.
- (41) de Araujo, W. R.; Frasson, C. M. R.; Ameku, W. A.; Silva, J. R.; Angnes, L.; Paixão, T. R. Single-Step Reagentless Laser Scribing Fabrication of Electrochemical Paper-Based Analytical Devices. *Angew. Chem.* **2017**, *129*, 15309–15313.
- (42) Ye, R.; Chyan, Y.; Zhang, J.; Li, Y.; Han, X.; Kittrell, C.; Tour, J. M. Laser-Induced Graphene Formation on Wood. *Adv. Mater.* **2017**, *29*, No. 1702211.
- (43) Chyan, Y.; Ye, R.; Li, Y.; Singh, S. P.; Arnusch, C. J.; Tour, J. M. Laser-Induced Graphene by Multiple Lasing: Toward Electronics on Cloth, Paper, and Food. *ACS Nano* **2018**, *12*, 2176–2183.
- (44) Ye, R.; Han, X.; Kosynkin, D. V.; Li, Y.; Zhang, C.; Jiang, B.; Martí, A. A.; Tour, J. M. Laser-Induced Conversion of Teflon into Fluorinated Nanodiamonds or Fluorinated Graphene. *ACS Nano* **2018**, *12*, 1083–1088.
- (45) Ye, R.; Peng, Z.; Wang, T.; Xu, Y.; Zhang, J.; Li, Y.; Niewski, L. G.; Lin, J.; Tour, J. M. In Situ Formation of Metal Oxide Nanocrystals Embedded in Laser-Induced Graphene. *ACS Nano* **2015**, *9*, 9244–9251.
- (46) Fenzl, C.; Nayak, P.; Hirsch, T.; Wolfbeis, O. S.; Alshareef, H. N.; Baumner, A. J. Laser-Scribed Graphene Electrodes for Aptamer-Based Biosensing. *ACS Sens.* **2017**, *2*, 616–620.
- (47) Tao, L. Q.; Tian, H.; Liu, Y.; Ju, Z. Y.; Pang, Y.; Chen, Y. Q.; Wang, D. Y.; Tian, X. G.; Yan, J. C.; Deng, N. Q.; et al. An Intelligent Artificial Throat with Sound-Sensing Ability Based on Laser Induced Graphene. *Nat. Commun.* **2017**, *8*, No. 14579.
- (48) Singh, S. P.; Li, Y.; Zhang, J.; Tour, J. M.; Arnusch, C. J. Sulfur-Doped Laser-Induced Porous Graphene Derived from Polysulfone-Class Polymers and Membranes. *ACS Nano* **2018**, *12*, 289–297.
- (49) Zang, X.; Shen, C.; Chu, Y.; Li, B.; Wei, M.; Zhong, J.; Sanghadasa, M.; Lin, L. Laser-Induced Molybdenum Carbide – Graphene Composites for 3D Foldable Paper Electronics. *Adv. Mater.* **2018**, *30*, No. e1800062.
- (50) Luong, D. X.; Subramanian, A. K.; Silva, G. A. L.; Yoon, J.; Cofer, S.; Yang, K.; Owuor, P. S.; Wang, T.; Wang, Z.; Lou, J.; et al. Laminated Object Manufacturing of 3D-Printed Laser-Induced Graphene Foams. *Adv. Mater.* **2018**, *30*, No. 1707416.
- (51) Strauss, V.; Marsh, K.; Kowal, M. D.; El-Kady, M.; Kaner, R. B. A Simple Route to Porous Graphene from Carbon Nanodots for Supercapacitor Applications. *Adv. Mater.* **2018**, *30*, No. 1704449.
- (52) Peng, Z.; Ye, R.; Mann, J. A.; Zakhidov, D.; Li, Y.; Smalley, P. R.; Lin, J.; Tour, J. M. Flexible Boron-Doped Laser-Induced Graphene Microsupercapacitors. *ACS Nano* **2015**, *9*, 5868–5875.
- (53) Clerici, F.; Fontana, M.; Bianco, S.; Serrapede, M.; Perrucci, F.; Ferrero, S.; Tresso, E.; Lamberti, A. In Situ MoS₂ Decoration of Laser-Induced Graphene as Flexible Supercapacitor Electrodes. *ACS Appl. Mater. Interfaces* **2016**, *8*, 10459–10465.
- (54) Zhang, W.; Xu, J.; Hou, D.; Yin, J.; Liu, D.; He, Y.; Lin, H. Hierarchical Porous Carbon Prepared from Biomass through a Facile Method for Supercapacitor Applications. *J. Colloid Interface Sci.* **2018**, *530*, 338–344.
- (55) Wang, J.; Kaskel, S. KOH Activation of Carbon-Based Materials for Energy Storage. *J. Mater. Chem.* **2012**, *22*, 23710–23725.

- (56) Liu, D.; Zhang, W.; Lin, H.; Li, Y.; Lu, H.; Wang, Y. A Green Technology for the Preparation of High Capacitance Rice Husk-Based Activated Carbon. *J. Cleaner Prod.* **2016**, *112*, 1190–1198.
- (57) Zhang, W.; Zhao, M.; Liu, R.; Wang, X.; Lin, H. Hierarchical Porous Carbon Derived from Lignin for High Performance Supercapacitor. *Colloids Surf., A* **2015**, *484*, 518–527.
- (58) Zhu, Y.; Murali, S.; Stoller, M. D.; Ganesh, K. J.; Cai, W.; Ferreira, P. J.; Pirkle, A.; Wallace, R. M.; Cychoz, K. A.; Thommes, M.; et al. Carbon-Based Supercapacitors Produced by Activation of Graphene. *Science* **2011**, *332*, 1537–1542.
- (59) Xu, J.; Tan, Z.; Zeng, W.; Chen, G.; Wu, S.; Zhao, Y.; Ni, K.; Tao, Z.; Ikram, M.; Ji, H.; et al. A Hierarchical Carbon Derived from Sponge-Templated Activation of Graphene Oxide for High-Performance Supercapacitor Electrodes. *Adv. Mater.* **2016**, *28*, 5222–5228.
- (60) Sevilla, M.; Fuertes, A. B. Direct Synthesis of Highly Porous Interconnected Carbon Nanosheets and Their Application as High-Performance Supercapacitors. *ACS Nano* **2014**, *8*, 5069–5078.
- (61) Puthusseri, D.; Aravindan, V.; Madhavi, S.; Ogale, S. 3D Micro-Porous Conducting Carbon Beehive by Single Step Polymer Carbonization for High Performance Supercapacitors: The Magic of in Situ Porogen Formation. *Energy Environ. Sci.* **2014**, *7*, 728–735.
- (62) Li, Y.; Li, Z.; Shen, P. K. Simultaneous Formation of Ultrahigh Surface Area and Three-Dimensional Hierarchical Porous Graphene-like Networks for Fast and Highly Stable Supercapacitors. *Adv. Mater.* **2013**, *25*, 2474–2480.
- (63) Yang, W.; Yang, W.; Ding, F.; Sang, L.; Ma, Z.; Shao, G. Template-Free Synthesis of Ultrathin Porous Carbon Shell with Excellent Conductivity for High-Rate Supercapacitors. *Carbon* **2017**, *111*, 419–427.
- (64) Largeot, C.; Portet, C.; Chmiola, J.; Taberna, P. L.; Gogotsi, Y.; Simon, P. Relation between the Ion Size and Pore Size for an Electric Double-Layer Capacitor. *J. Am. Chem. Soc.* **2008**, *130*, 2730–2731.
- (65) Jin, H.; Li, J.; Yuan, Y.; Wang, J.; Lu, J.; Wang, S. Recent Progress in Biomass-Derived Electrode Materials for High Volumetric Performance Supercapacitors. *Adv. Energy Mater.* **2018**, *8*, No. 1801007.
- (66) Song, Y.; Liu, T.; Qian, F.; Zhu, C.; Yao, B.; Duoss, E.; Spadaccini, C.; Worsley, M.; Li, Y. Three-Dimensional Carbon Architectures for Electrochemical Capacitors. *J. Colloid Interface Sci.* **2018**, *509*, 529–545.
- (67) Zhang, W.; Lin, H.; Lin, Z.; Yin, J.; Lu, H.; Liu, D.; Zhao, M. 3D Hierarchical Porous Carbon for Supercapacitors Prepared from Lignin through a Facile Template-Free Method. *ChemSusChem* **2015**, *8*, 2114–2122.